Phase-Locking Parametric Instability Coupling Longitudinal and Transverse Waves on Rivulets in a Hele-Shaw Cell

Grégoire Le Lay* and Adrian Daerr
Matière et Systèmes Complexes UMR 7057 CNRS, Université Paris Cité, 75231 Paris cedex 13, France

(Received 9 January 2024; accepted 25 November 2024; published 6 January 2025)

We report an instability exhibited by a fluid system when coupling two distinct types of waves, both linearly damped. While none of them is unstable on its own, they amplify one another, resulting in a previously unreported convective instability. An external excitation is used to induce a parametric cross-coupling between longitudinal and transverse deformations of a liquid bridge between two vertical glass plates. Coherent amplification results in waves satisfying a synchronization condition, which selects a precise wavelength. We derive a model for this instability using depth-averaged Navier-Stokes equations, showing the physical origin of the coamplification, and confirm its relevance experimentally. Our findings open new perspectives in the study of parametrically controlled pattern formation, and invites the search for analogous parametric cross-coupling instabilities in other systems exhibiting distinct wave types, from plasma to elastic media.

DOI: 10.1103/PhysRevLett.134.014001

For more than one and a half centuries, the study of hydrodynamic instabilities has driven our understanding of dynamical systems, and led to the development of tools to tackle nonlinear systems with many degrees of freedom that are used in all realms of physics and indeed all sciences. Examples of hydrodynamic instabilities include the laminar-to-turbulent transition [1], the Rayleigh-Plateau instability of a liquid cylinder [2], or the Kelvin-Helmholtz instability of the interface between fluid phases moving relative to one another, as in wind blowing over water giving rise to waves [3]. Understanding these instabilities is of tremendous importance in environmental, biological, and other natural settings, as well as in many industrial processes, where the instability can be desirable as in combustion or printing or deleterious as in coating [4].

This Letter reports on an original parametric instability that should be relevant in many contexts outside hydrodynamics. Parametric instabilities arise from the temporal variation of a multiplicative parameter. In hydrodynamics (Faraday instability of an accelerated liquid [5]) or optics (parametric amplification of optical signals [6]), this variation usually creates a nonlinear coupling of a wave field to itself (surface height and electric field, respectively, in the given examples). In contrast, the instability described here involved the coupling of two distinct wave types, which do not interact in the absence of external forcing. The parametric coupling of distinct modes can also occur in plasma, e.g., Langmuir and ion acoustic waves, under the effect of an external dipolar field [7,8]. As a multitude of physical systems can sustain distinct wave types (e.g., compressive and shear waves in elastic media), we expect that analogous nonlinear wave coupling instabilities may occur in other very different contexts from geophysics and acoustics to astrophysics.

Here, we subject a liquid filament, henceforth termed "rivulet," to homogeneous acoustic forcing, and describe a previously unreported instability where the path followed by the rivulet becomes sinuous, while simultaneously the streamwise mass distribution becomes inhomogeneous. We show that both features, although damped under normal conditions, grow by amplifying one another through a parametric coupling created by the acoustic forcing. When the difference between fluid advection velocity and sinusoidal wave speed precisely matches the ratio of perturbation wavelength and period, the coupling becomes coherent and phase-locked, leading to reciprocal amplification. For the sake of clarity we stress that this cross-coupling and its parametric origin is the original finding of this Letter, and fundamentally distinguishes the resulting instability from the unforced, inertial meandering instability occurring above a threshold flow rate [9,10].

Experimental setup—We inject liquid between two vertical and parallel glass plates separated by a gap of air of thickness $b = 0.6$ mm, forming a Hele-Shaw cell. The liquid (perfluorinated polyether PFPE, Galden HT135, density $\rho = 1.71$ g/ml, surface tension $\gamma = 17$ mN/m, kinematic viscosity $\nu = 1$ mm^2/s) totally wets the glass. The liquid forms a bridge joining the plates and falling downward. Since the plate separation b is chosen inferior to the capillary length, the bridge is in first approximation bounded by semicylindrical interfaces meeting the glass with vanishing contact angle [11].

*Contact author: gregoire.le-lay@u-paris.fr

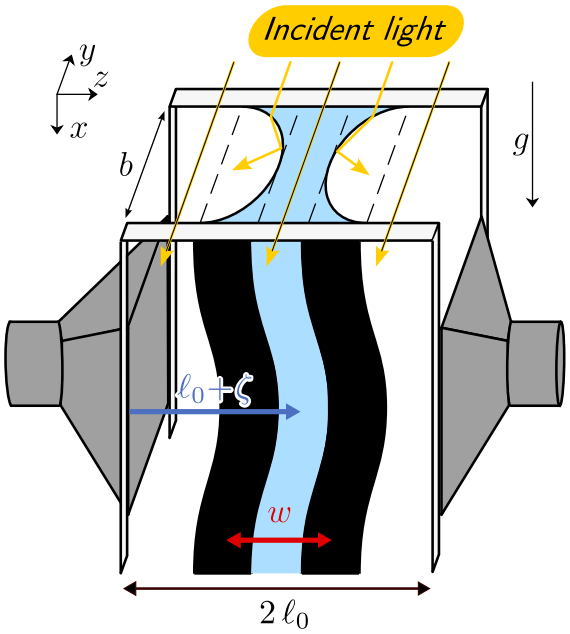

FIG. 1. Sketch of the experimental apparatus, not to scale. The glass panes are 1 m high and 30 cm wide, and set $b = 0.6$ mm apart. The lateral boundaries are closed except for a 20 cm range, vertically centered, where loudspeakers impose the pressure. When viewed head on, the rivulet appears delimited by dark bands where the curved interface refracts light away from the optical axis.

The liquid is injected into the cell through a pipette tip fed by a gear pump. Underneath the cell the fluid falls into a container that is continuously weighed, allowing us to measure the flow rate Q.

We use a camera to look at the rivulet, which is backlit with quasicollimated light. The two regions of curved menisci appear as dark bands on a bright background, framing a central light band where light passes unhindered through the bulk (Fig. 1). This allows us to record the position of both the menisci as a function of x, from which we define the rivulet position $\zeta(x,t)$ as the middle of the bright region and the rivulet width $w(x,t)$ as the distance between the two menisci. By measuring the width of the dark regions, we are also able to know if the menisci are still semicircular or have been deformed.

When not subject to forcing, the rivulet flows straight vertically or exhibits spontaneous meandering depending on whether the flow rate is inferior or superior to a critical flow rate Q^*, the origin of which has been studied previously [10]. In both cases, the rivulet is always observed to be of constant width. Indeed, since the curvature of the interface in the transverse (y,z) plane is fixed by the cell spacing, the rivulet is not subjected to the Plateau-Rayleigh instability and any variation in width is linearly damped.

The rivulet behaves as a one-dimensional membrane effectively splitting the cell in two regions, into which we force air using speakers on the sides of the cell (Fig. 1) driven by a sinusoidal signal of frequency f_0 in a push-pull configuration: when one speaker pushes air into the space on the left of the rivulet, the other draws air on the right, and the process is reversed half a period later. Since the acoustic wavelength in air corresponding to the frequency used is always larger than the cell width, the rivulet is subjected to spatially homogeneous forcing over a region spanning 20 cm lengthwise. The neutral line around which the rivulet oscillates can display a small shift in the z direction, with respect to the path in the absence of forcing, over the scale of the excited portion of the cell. This is a consequence of a slight asymmetry in amplitude of the movements induced by the two speakers.

Results—At leading order, the rivulet responds to the forcing by moving sideways, i.e., along z, harmonically. At low to moderate frequencies we observe that inertia is negligible, that is, the rivulet displacement is in phase with that of the loudspeaker membranes. This sideways movement of the whole rivulet at the forcing frequency is always present, as indicated by the displacement relative to the blue dashed line in Fig. 2. In the experiments that follow, we induced transverse displacements of 0.2–2 mm, depending on the frequency.

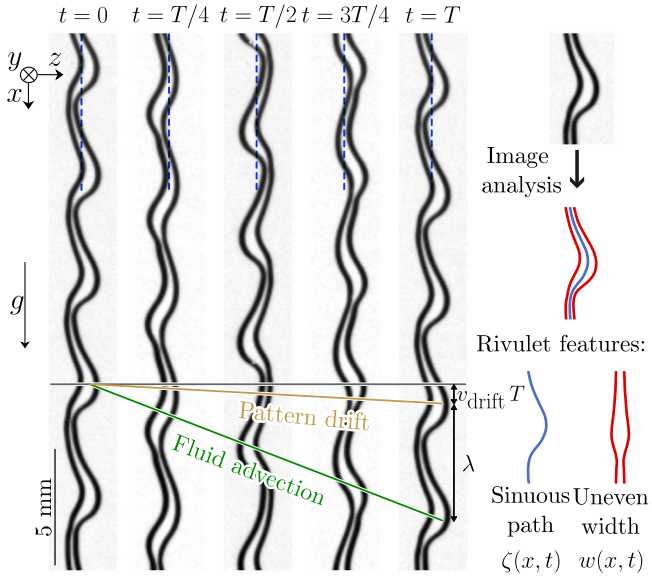

FIG. 2. Left: snapshots of the rivulet over one forcing period $T = 20$ ms, for $Q > Q^*$ ($Q = 46 \pm 1$ mm^3/s). The phase velocity v_{drift} of the sinuous deformation is smaller than that at which the liquid bulges flow downstream. Note how the pattern reproduces exactly after one period T, up to a translation. The dashed blue line represents the position of the rivulet averaged in time and space. The spatially averaged (over x) rivulet position coincides with this line at $t = 0, T/2, T$ and the rivulet is off-centered on the left at $t = T/4$ and symmetrically on the right at $t = 3T/4$. Right: decomposition of the rivulet profile into the z-wise deformation of the center line (ζ, in blue) and the width modulation (w, in red).

On top of this synchronous sideways movement, when the forcing amplitude is above a certain threshold that depends on the forcing frequency, the rivulet adopts a sinuous trajectory with a well-defined wavelength λ that is orders of magnitude below the acoustic wavelength. Moreover, the width of the rivulet is also modulated with the same spatial periodicity (Fig. 2 and movie S1 [12]; such a modulation is sometimes termed "varicose mode" in the literature). Movie S2 shows the initial growth after the onset of forcing, while movie S3 shows how the perturbations quickly decay when the excitation is switched off.

The width modulations are advected streamwise at a velocity only weakly depending on frequency and flow rate, whereas the sinuous pattern is either static or drifts slowly at a drift speed v_{drift}, which can be zero, positive, or negative and that depends on the forcing frequency and the flow rate (Fig. 3 inset).

This reorganization of the rivulet is observed for a wide range of frequencies (10–1000 Hz). The wavelength nears the system size at the low end of this range, and drops below the gap size b and optical resolution at high frequencies, indicating that the frequency range of observable response could be extended even further through appropriate modifications of the setup.

When the drift speed is zero, we observe that the rivulet profile is exactly the same, both in lateral displacement and width, every period T. This also holds, up to a translation in x, when the drift speed is nonzero (Fig. 2). In other terms the path and width modulations are phase-locked. This suggests that the wavelength selection is given by the relative speed of the width modulation with respect to the path modulation: after one period, compared to the path modulation, the width modulation has traveled exactly one wavelength further downstream. The wavelength thus acts as a degree of freedom that allows the rivulet to respond to any forcing frequency (movie S1).

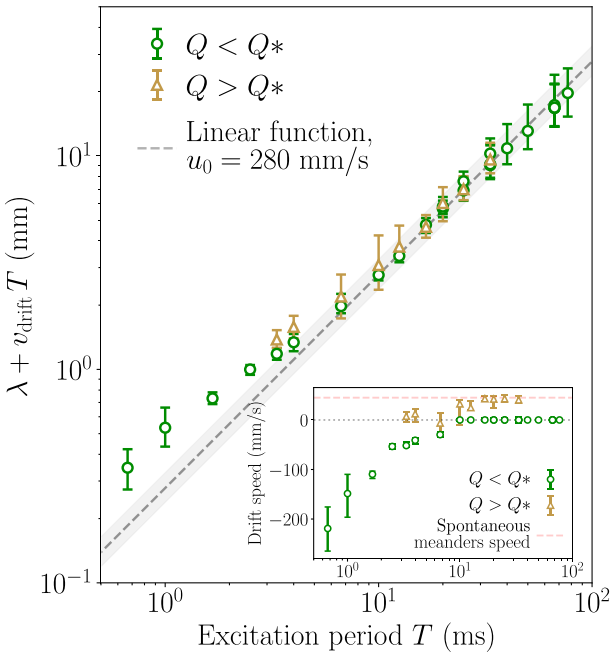

FIG. 3. The distance traveled over one period by the width modulation as a function of the forcing period for two flow rates Q, 26 ± 1 mm^3/s and 46 ± 1 mm^3/s, being respectively below and above the spontaneous meandering threshold Q^*. The dashed line is the linear function of slope u_0. Inset: sinuous pattern drift speed v_{drift} as a function of the forcing period.

This is remarkably confirmed by plotting the distance traveled by the width modulation, i.e., the wavelength λ plus path drift distance in one period $v_{\mathrm{drift}}T$, as a function of the external forcing period T (Fig. 3). Assuming the phase speed of the width modulations matches the bulk (Darcy) flow speed $u_0 = gb^2/(12\nu) = 280 \pm 40$ mm/s, one expects the relation $\lambda + v_{\mathrm{drift}}T = u_0 T$ to hold. We find quantitative agreement over 2 orders of magnitude with this prediction without any adjustable parameter.

The points are slightly offset from the curve for periods smaller than 4 ms, an effect that we attribute to the meniscus deformation. Indeed, the semicircular shape of the meniscus is maintained for slow rivulet movements, but viscous dissipation changes the dynamic contact angle on the glass significantly for faster motion. When the rivulet is subjected to fast transverse movements, the interface flattens where the fluid advances, while the concavity increases where it retreats. For this reason, at high frequencies we experimentally observe the interface to become noncircular, with the meniscus shadows showing time oscillating asymmetry (not shown). We thus expect the average viscous dissipation to differ from the semicylindrical meniscus case, affecting the fluid velocity and/or the sinuous drift velocity.

The measured drift speed of the path modulation (Fig. 3 inset) shows a nontrivial behavior: for flow rates below the spontaneous meandering threshold ($Q < Q^*$) the sinuous pattern is stationary for frequency below 100 Hz, and drifts upstream at higher frequencies. For flow rates above Q^* and at low frequencies, the sinuous pattern moves downstream at the spontaneous meanders' phase speed, which we measure independently in the absence of forcing.

Discussion—In this section we propose a model for the rivulet dynamics, based on the dominant physical ingredients. We identify the mechanism for the unstable cross-amplification of phase-locked path and width modulations.

The action of the speakers can be taken as equivalent to that of two infinite rigid vertical walls placed symmetrically at distance $\pm \ell_0$ from the rest position of the straight rivulet at $\zeta = 0$, moving horizontally so that their position relative to the situation at rest is given by $Z(t) = Z_0 \cos(2\pi f_0 t)$, and acting like pistons on the air to the left and right of the rivulet. From Mariotte's law, for small displacements it follows that the force per unit length exerted on the rivulet is $b\rho\Pi(Z - \langle\zeta\rangle_x)$ with $\Pi = 2P_0/(\rho\ell_0)$, where P_0 is the

atmospheric pressure and $\langle\zeta\rangle_x$ is the space-averaged position of the rivulet. Thus the rivulet behavior is given by

$$w(\partial_t+\beta\mathbf{u}\cdot\boldsymbol{\nabla})\mathbf{u}=w\mathbf{g}-w\mu\mathbf{u}+w\Gamma\boldsymbol{\nabla}(\partial_{xx}w)+\left[\Gamma\partial_{xx}\zeta-\mu_{\mathrm{cl}}\mathbf{u}\cdot\mathbf{n}+\Pi(Z-\langle\zeta\rangle_x)\right]\mathbf{n}, \tag{1}$$

$$(\partial_t+\mathbf{u}\cdot\boldsymbol{\nabla})w=-w\boldsymbol{\nabla}\cdot\mathbf{u}. \tag{2}$$

The first equation is the depth-averaged Navier-Stokes equation integrated over the width of the rivulet w, where $\mathbf{u}=u\mathbf{e}_x+v\mathbf{e}_z$ is the fluid velocity and $\mathbf{n}$ is a unit vector normal to the rivulet path ζ. The second equation reflects mass conservation.

The lhs of Eq. (1) represents inertia, where the numerical prefactor $\beta\simeq 1$ accounts for the velocity's y profile. Henceforth, following [10], we take $\beta=1$ to simplify the equations without losing physical relevance. The terms on the right represent, in this order, gravity, viscous friction internal to the rivulet following from Darcy's law with $\mu=12\nu/b^2$, streamwise Laplace pressure gradient inside the rivulet due to width variations and forces normal to the rivulet center line. Note that the streamwise Laplace pressure gradient tends to regularize width variations, unlike in the Rayleigh-Plateau instability of cylindrical filaments.

The last term includes three contributions of normal forces. Surface tension γ tends to straighten the rivulet, with $\partial_{xx}\zeta$ being the curvature of the rivulet in the (x,z) plane and $\Gamma=\pi\gamma/(2\rho)$ [11]. The second term makes for contact line friction, accounting for the high dissipation at the meniscus edges when the rivulet slides transversally on thin films of thickness $h\ll b$ on the plates outside the rivulet: $\mu_{\mathrm{cl}}\approx b\mu\sqrt{b/h}$ ([10], to be published), with $h=3$ μm for $Q=46\pm1$ mm^3/s. The last term is the acoustic pressure discussed above.

The base solution is a straight rivulet of constant width w_0, located at $z=\zeta_0(t)$ with velocity $\mathbf{u}=[u_0=g/\mu, v_0=\partial_t\zeta_0(t)]$. The rivulet rest width w_0 in the experimental results presented here was measured to be 0.22 ± 0.04 mm for $Q=26\pm1$ mm^3/s and 0.33 ± 0.04 mm for $Q=46\pm1$ mm^3/s. To understand the mechanism leading to the instability we consider a weak perturbation of this straight rivulet with $u=u_0+\epsilon u_1(x,t)$, $w=w_0+\epsilon w_1(x,t)$, and $\zeta=\zeta_0(t)+\epsilon\zeta_1(x,t)$. The transverse speed is $v=(\partial_t+\mathbf{u}\cdot\nabla)\zeta$. The Navier-Stokes Eq. (1) projected on $\mathbf{e}_z$ gives at order 0

$$w_0(\partial_t+\mu)\partial_t\zeta_0=-\mu_{\mathrm{cl}}\partial_t\zeta_0+\Pi(Z-\zeta_0)=:w_0F(t). \tag{3}$$

This equation describes the back and forth membranelike movement of the rivulet. It is linear in the forcing amplitude, and indeed the experimental space-averaged rivulet position ζ_0 is always well fitted by a sine function of time.

At order 1 the same projection yields an equation governing the fluid path ζ,

$$[w_0(\partial_t+u_0\partial_x)(\partial_t+u_0\partial_x+\mu)-\Gamma\partial_{xx}+\mu_{\mathrm{cl}}\partial_t]\zeta_1=-Fw_1, \tag{4}$$

which corresponds to Eq. (4) from [10] with an extra forcing term on the rhs. This term couples the purely time-dependent forcing F and the width w, which is advected at speed u_0. It is destabilizing and causes width modulations in conjunction with acoustic forcing to amplify path perturbations.

By projecting Eq. (1) on $\mathbf{e}_x$, we obtain at first order in ϵ the evolution equation for the width w,

$$[(\partial_t+u_0\partial_x)(\partial_t+u_0\partial_x+\mu)+w_0\Gamma\partial_{xxxx}]w_1=w_0F\partial_{xx}\zeta_1. \tag{5}$$

The right-hand term can be understood as a stretching or compression of curved rivulet segments by the pressure difference across the rivulet. This term implies that the growth of width perturbations is a consequence of path modulations combined with acoustic forcing.

An interesting property of Eqs. (4) and (5) is that the destabilizing rhs does not contain the quantity differentiated on the lhs. In other words neither the sinuosity ζ_1 nor the width variations w_1 are directly amplified by the excitation forcing, but rather the acoustic forcing allows mutual growth by cross-coupling the two modes. While a coupling between sinuous and width variation modes is not unusual and is found for example in jets [13,14], usually both modes are intrinsically unstable, can exist on their own, and compete against each other. Here, sinuous and width perturbations are linearly damped when considered independently, i.e., in the absence of forcing-induced coupling. They grow only by sustaining one another through parametric coupling.

We can find experimental confirmation of this mechanism by looking at the spatiotemporal Fourier transform of the position and width of the rivulet. Using image analysis tools, we extract from the video the width and the position of the rivulet as a function of time and the x coordinate (Fig. 2 right, Figs. SF2 and SF3). In Fig. 4 and Fig. S1 we represent the logarithm of the power spectrum of ζ and w in the reciprocal space (q,f). Zones of high intensity are organized in localized spots because of the quasiperiodicity of the pattern. For nonzero wave numbers, the more intense harmonics are at positive frequencies, corresponding to positive speed (downward displacement).

More can be said from Fig. 4 and Fig. S1 on the spatiotemporal behavior of the rivulet. For instance, note how for $q=0$, the displacement spectrum $\hat{\zeta}$ has peaks (blue

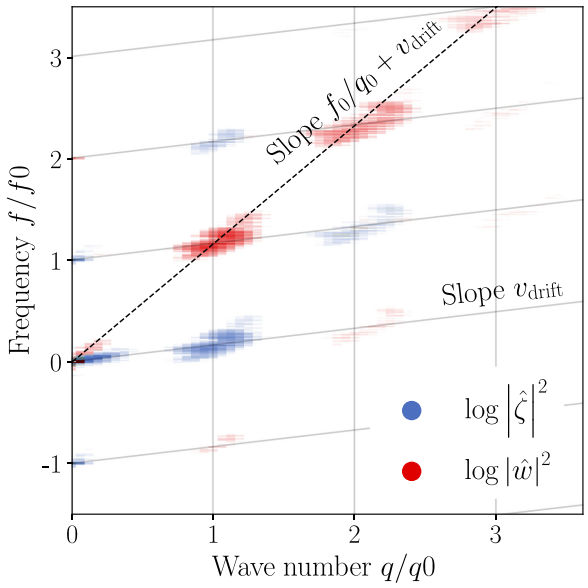

FIG. 4. Spatiotemporal power spectrum of the position (blue) and width (red) of the rivulet for $Q > Q^*$ ($Q = 46 \pm 1$ mm^3/s). The frequency scale is set by the forcing frequency $f_0 = 50$ Hz, the wave number scale by the dominant mode $q_0 = 0.193$ mm^{-1}. The color intensity indicates the strength of the signal on a logarithmic scale, with a cutoff to white below -110 dB of the peak signal. An equivalent plot for a lower flow rate $Q < Q^*$ is included in the Supplemental Material [12] as Fig. S1.

patches) at $\pm f_0$ but not at $\pm n f_0$ with $n > 1$: this reflects the fact that the space-averaged response of the rivulet is linear and the global movement of the filet $\zeta_0(t)$ is sinusoidal in time, in accordance with Eq. (3).

More importantly, the patches of highest power in $\hat{w}$ (red) lie on a line whose slope is the speed of the width modulations. The relevance of the mutual amplification mechanism described above is supported by the fact that on a given vertical line the high-signal regions alternate between $\hat{w}$ (red) and $\hat{\zeta}$ (blue), the gap between two consecutive spots being the forcing frequency f_0. This shows that both modes are coupled by a function oscillating at f_0, and that no mode is unstable on its own (or we would see all its time harmonics). Finally the localization of the spectrum at discrete wave numbers is also explained by our model, positive feedback, and mutual amplification of longitudinal and transverse waves requiring the resonance condition $u_0 q = v_{\mathrm{drift}} q + n f_0$ to be met.

Conclusion and perspectives—Under the effect of a spatially uniform forcing, a homogeneous membrane or string is expected to respond by homogeneous transverse translation. Remarkably, the liquid rivulet studied in this Letter develops a pattern with a well-defined wavelength combining transverse deformations of the flow path and longitudinal modulations of the local cross section.

It is far from obvious that the added degree of freedom with respect to a string, namely the possibility to redistribute mass along the rivulet, should lead to an instability. Indeed both modes growing simultaneously, sinuosity and width variations, are linearly damped, and they amplify one another only when coupled by the forcing. This contrasts with vibrated soap films and strings loaded with beads, where mass redistribution merely causes the broadening of resonances [15,16].

Interestingly, although the acoustic forcing is additive, the effective forcing felt by the sinuosity and width variations is multiplicative. Formally this parametric cross-coupling is reminiscent of the way standing waves in the annular Faraday instability can be seen as arising through the coupling of counterpropagating waves [5]. The resonance condition to the amplification indicates a possible connection with the energy transfer due to resonant three-wave interaction in the case of stratified or homogeneous free-surface flows over a nonflat bottom [17,18].

The selection of the pattern drift speed is an open problem. We attributed modifications of the width advection speed at high frequencies to asymmetric deformations of the rivulet cross section. The study of these deformations, which can lead to rivulet breaking, could open the perspective of investigating the problem of the behavior of an air-fluid interface in a Hele-Shaw cell in the oscillating regime where inertial effects can be as important as capillary ones [19]. The forced rivulet also allows the coupling and simultaneous study of both the retreating and advancing menisci.

As an experimental investigation of a previously unreported instability, validated by theoretical modeling that identifies the mechanism as a new type of parametric coupling, this Letter opens exciting perspectives for new research and applications. The generation of wavelengths that are orders of magnitude smaller than the acoustic wavelength of the forcing could be exploited for controlled liquid fragmentation, mixing, and micromanufacturing. We also expect fundamental research on dynamical wetting to take advantage of the broad frequency response, that can for instance be used to probe timescales relevant in surfactant diffusion, adsorption, and desorption dynamics.

Acknowledgments—We thank Michael Berhanu and Chi-Tuong Pham for insightful discussions. The research received special funds from laboratory MSC UMR 7057.

[1] M. Avila, D. Barkley, and B. Hof, Annu. Rev. Fluid Mech. **55**, 575 (2023).
[2] J. Eggers and E. Villermaux, Rep. Prog. Phys. **71**, 036601 (2008).
[3] M. Rabaud and F. Moisy, C. R. Méc. **348**, 489 (2020).
[4] F. Charru, *Hydrodynamic Instabilities*, Cambridge Texts in Applied Mathematics (Cambridge University Press, Cambridge, England, 2011).
[5] S. Douady, S. Fauve, and O. Thual, Europhys. Lett. **10**, 309 (1989).

[6] S. A. Akhmanov, A. I. Kovrigin, A. S. Piskarskas, V. V. Fadeev, and R. V. Khokhlov, Zh. Eksp. Teor. Fiz. **45**, 1336 (1965) [Sov. J. Exp. Theor. Phys. Lett. **18**, 191 (1965)], http://jetp.ras.ru/cgi-bin/e/index/e/18/4/p919?a=list.
[7] K. Nishikawa, J. Phys. Soc. Jpn. **24**, 916 (1968).
[8] C. Liu and V. Tripathi, Phys. Rep. **130**, 143 (1986).
[9] W. Drenkhan, H. Ritacco, A. Saint-Jalmes *et al.*, Phys. Fluids **19**, 102101 (2007).
[10] A. Daerr, J. Eggers, L. Limat, and N. Valade, Phys. Rev. Lett. **106**, 184501 (2011).
[11] C.-W. Park and G. M. Homsy, J. Fluid Mech. **139**, 291 (1984).
[12] See Supplemental Material at http://link.aps.org/supplemental/10.1103/PhysRevLett.134.014001 for movies showing the rivulet oscillating, the start, and the end of the instability; as well as figures showing the spatio-temporal evolution of the position and width of the rivulet and a figure similar to Fig. 4 for $Q < Q^*$.
[13] K. Mikhaylov and X. Wu, Phys. Fluids **32**, 064104 (2020).
[14] S. J. Leib and M. E. Goldstein, Phys. Fluids **1**, 513 (1989).
[15] A. Boudaoud, Y. Couder, and M. Ben Amar, Eur. Phys. J. B **9**, 159 (1999).
[16] A. Boudaoud, Y. Couder, and M. Ben Amar, Phys. Rev. Lett. **82**, 3847 (1999).
[17] E. S. Benilov, J. Fluid Mech. **185**, 551 (1987).
[18] R. A. D. Szoeke, J. Fluid Mech. **130**, 279 (1983).
[19] P. Aussillous and D. Quéré, Phys. Fluids **12**, 2367 (2000).